JMEPEG (2010) 19:942–950
DOI: 10.1007/s11665-009-9570-z

1059-9495/$19.00

Modeling of the Weld Shape Development During the Autogenous Welding Process by Coupling Welding Arc with Weld Pool

Wenchao Dong, Shanping Lu, Dianzhong Li, and Yiyi Li

(Submitted November 17, 2008; in revised form August 25, 2009)

A numerical model of the welding arc is coupled to a model for the heat transfer and fluid flow in the weld pool of a SUS304 stainless steel during a moving GTA welding process. The described model avoids the use of the assumption of the empirical Gaussian boundary conditions, and at the same time, provides reliable boundary conditions to analyze the weld pool. Based on the two-dimensional axisymmetric numerical modeling of the argon arc, the heat flux to workpiece, the input current density, and the plasma drag stress are obtained. The arc temperature contours, the distributions of heat flux, and current density at the anode are in fair agreement with the reported experimental results. Numerical simulation and experimental studies to the weld pool development are carried out for a moving GTA welding on SUS304 stainless steel with different oxygen content from 30 to 220 ppm. The calculated result show that the oxygen can change the Marangoni convection from outward to inward direction on the liquid pool surface and make the wide shallow weld shape become narrow deep one. The calculated result for the weld shape and weld D/W ratio agrees well with the experimental one.

Keywords Marangoni convection, numerical simulation, weld shape, welding arc and weld pool

1. Introduction

Since 1980s, great attentions have been paid to activating flux tungsten inert gas (A-TIG) welding for improving the efficiency of TIG welding (Ref 1-10), which was first developed by Paton Electric Welding Institute in the 1960s (Ref 1). Even though some fluxes for the A-TIG process are commercially available and have been applied in industry, there is still no commonly agreed mechanism for the increase in penetration depth (Ref 5, 6). Up to now, the four representative theories, namely, the TIG keyhole mode (Ref 2), the arc constriction (Ref 3-5), the reversal of the Marangoni convection in the weld pool (Ref 6-10), and the insulation mode (Ref 11) were proposed. The main reason is that the weld shape development depends to a large extent on the fluid flow in liquid pool, which is controlled by the plasma drag force, surface tension, electromagnetic force, and buoyancy at the same time, and the affecting factors not only relate to the arc physics but also depend on the liquid pool physical metallurgy. Therefore, in recent decades, numerical calculations of heat transfer and fluid flow have been utilized to understand various weld characteristics that cannot be obtained by the experiment otherwise. Oreper and Szekely (Ref 12) used dimensionless analysis and numerical modeling to understand the role of conduction and convection in the weld pool. Zacharia et al. (Ref 13, 14), Wang et al. (Ref 15), and Zhang and Fan (Ref 16) developed a multidimensional mathematical model to simulate the convection and heat transfer of a stationary GTA welding pool, considering the surface tension temperature gradient as a function of temperature and sulfur or oxygen concentration.

In fact, the welding arc and weld pool coexist and depend on each other in the welding process. But many studies separated the welding arc and weld pool in the published papers. The model built in these papers used unreliable boundary conditions for the heat flux or current density on the pool surface, which was considered as the assumption of the empirical Gaussian. Moreover, the shear stress is neglected in the model because it is difficult to obtain from the experiment. In our previous study (Ref 17), by comparing the calculation and the experiment for weld shape, there are still some differences at the size of the weld shape. The main reason is that the plasma drag force is not considered. It is seen that the effect of the welding arc on the weld shape must be considered. Tanaka et al. (Ref 18) treating tungsten cathode, arc plasma, and anode as a unified model obtained the results that the convection flow in the liquid pool is dominated by the plasma drag force and the Marangoni force during pure argon shielded GTA welding. However, the effect of surface active element on the Marangoni convection and weld shape in his paper is not discussed in detail.

In this study, a mathematical model by combining the welding arc and weld pool for the moving GTA welding on SUS304 stainless steel is established by using FLUENT software. To provide reliable boundary condition for analyzing of weld pool, the welding arc is calculated at first. Some arc properties including the temperature contours, the heat flux, and

Wenchao Dong, Shanping Lu, Dianzhong Li, and **Yiyi Li**, Shenyang National Laboratory for Materials Science, Institute of Metal Research, Chinese Academy of Sciences, 72 Wenhua Road, Shenyang 110016, China. Contact e-mails: wcdong@imr.ac.cn and shplu@imr.ac.cn.

current density on the anode surface between the calculation and the experiment are compared for validating the welding arc. And then the heat flux, current density, and shear stress from the welding arc model are used as the boundary conditions of the molten pool and systematically investigated the effect of the surface active element oxygen on the Marangoni convection and weld shape by considering the buoyancy, electromagnetic force, surface tension as a function of temperature and oxygen concentration and the plasma drag force. Finally, the numerical results for the weld shape and weld D/W ratio are compared with the experimentally observed one.

2. Mathematical Model

2.1 Assumptions

To simplify the mathematical model, the following assumptions have been made:

(1) The arc plasma is assumed to be 2D axisymmetric.
(2) The weld pool is assumed to be 3D symmetric along y-z plane.
(3) Gas and liquid metal are incompressible and the flow is laminar.
(4) The arc is assumed to be pure argon in local thermodynamic equilibrium (LTE).

2.2 Governing Equations

2.2.1 Mathematical Formulation of the Welding Arc. Based on the above assumptions, the conservation equations for the welding arc can be expressed as follows (Ref 19).

Continuity:

$$\frac{\partial(\rho_{\mathrm{Ar}}v_z)}{\partial z}+\frac{1}{r}\frac{\partial(\rho_{\mathrm{Ar}}rv_r)}{\partial r}=0 \qquad \text{(Eq 1)}$$

Axial momentum:

$$\frac{\partial(\rho_{\mathrm{Ar}}v_zv_z)}{\partial z}+\frac{1}{r}\frac{\partial(\rho_{\mathrm{Ar}}rv_rv_z)}{\partial r}=-\frac{\partial p}{\partial z}+\frac{\partial}{\partial z}\left(2\mu_{\mathrm{Ar}}\frac{\partial v_z}{\partial z}\right)+\frac{1}{r}\frac{\partial}{\partial r}\left[r\mu_{\mathrm{Ar}}\left(\frac{\partial v_z}{\partial r}+\frac{\partial v_r}{\partial z}\right)\right]+j_rB_\theta \qquad \text{(Eq 2)}$$

Radial momentum:

$$\frac{\partial(\rho_{\mathrm{Ar}}v_zv_r)}{\partial z}+\frac{1}{r}\frac{\partial(\rho_{\mathrm{Ar}}rv_rv_r)}{\partial r}=-\frac{\partial p}{\partial r}+\frac{\partial}{\partial z}\left[\mu_{\mathrm{Ar}}\left(\frac{\partial v_r}{\partial z}+\frac{\partial v_z}{\partial r}\right)\right]+\frac{1}{r}\frac{\partial}{\partial r}\left(2r\mu_{\mathrm{Ar}}\frac{\partial v_r}{\partial r}\right)-j_zB_\theta \qquad \text{(Eq 3)}$$

Energy:

$$\frac{\partial(\rho_{\mathrm{Ar}}v_zh)}{\partial z}+\frac{1}{r}\frac{\partial(\rho_{\mathrm{Ar}}rv_rh)}{\partial r}=\frac{\partial}{\partial z}\left(\frac{k_{\mathrm{Ar}}}{C_{p,\mathrm{Ar}}}\frac{\partial h}{\partial z}\right)+\frac{1}{r}\frac{\partial}{\partial r}\left(r\frac{k_{\mathrm{Ar}}}{C_{p,\mathrm{Ar}}}\frac{\partial h}{\partial r}\right)+\frac{j_z^2+j_r^2}{\sigma_{\mathrm{Ar}}}-S_R+\frac{5}{2}\frac{k_{\mathrm{b}}}{e}\left(\frac{j_z}{C_{p,\mathrm{Ar}}}\frac{\partial h}{\partial z}+\frac{j_r}{C_{p,\mathrm{Ar}}}\frac{\partial h}{\partial r}\right) \qquad \text{(Eq 4)}$$

Charge continuity:

$$\frac{\partial}{\partial z}\left(\sigma_{\mathrm{Ar}}\frac{\partial\phi}{\partial z}\right)+\frac{1}{r}\frac{\partial}{\partial r}\left(r\sigma_{\mathrm{Ar}}\frac{\partial\phi}{\partial r}\right)=0 \qquad \text{(Eq 5)}$$

where ρ_{Ar}, k_{Ar}, μ_{Ar}, $C_{p,\mathrm{Ar}}$, and σ_{Ar} are the density, thermal conductivity, viscosity, specific heat, and electrical conductivity of argon, respectively. v_z and v_r are the axial and radial velocities. j_z and j_r are the axial and radial component of the current density. k_{b} is the Boltzmann constant (1.3807×10^{-23} m^2 kg/s^2/K), e is the electronic charge (1.6022×10^{-19} C), B_θ is the azimuthal magnetic field, h is the enthalpy, p is the pressure, and ϕ is the electric potential.

The last term in Eq 2 and 3 are the axial and radial electromagnetic body force term, respectively. The last three terms in Eq 4 represent Joule heating, the radiation losses, and the diffusive transport of enthalpy due to the electron flux, respectively.

To calculate the electromagnetic field and current densities, the vector potential method (Ref 20) and Ohm's law are needed:

$$j_z=-\sigma_{\mathrm{Ar}}\frac{\partial\phi}{\partial z},\quad j_r=-\sigma_{\mathrm{Ar}}\frac{\partial\phi}{\partial r} \qquad \text{(Eq 6)}$$

$$\frac{\partial^2A_z}{\partial z^2}+\frac{1}{r}\frac{\partial}{\partial r}\left(r\frac{\partial A_z}{\partial r}\right)+\mu_0j_z=0 \qquad \text{(Eq 7)}$$

$$\frac{\partial^2A_r}{\partial z^2}+\frac{1}{r}\frac{\partial}{\partial r}\left(r\frac{\partial A_r}{\partial r}\right)-\frac{A_r}{r^2}+\mu_0j_r=0 \qquad \text{(Eq 8)}$$

$$B_\theta=\frac{\partial A_r}{\partial z}-\frac{\partial A_z}{\partial r} \qquad \text{(Eq 9)}$$

where A_z and A_r are the axial and radial electrical vector potential, respectively. μ_0 is the magnetic permeability of free space (1.26×10^{-6} H/m).

2.2.2 Mathematical Formulation of the Weld Pool. Based on the above assumptions, the conservation equations for the weld pool can be expressed as follows (Ref 21).

Continuity:

$$\frac{\partial\rho_{\mathrm{m}}}{\partial t}+\frac{\partial(\rho_{\mathrm{m}}u)}{\partial x}+\frac{\partial(\rho_{\mathrm{m}}v)}{\partial y}+\frac{\partial(\rho_{\mathrm{m}}w)}{\partial z}=0 \qquad \text{(Eq 10)}$$

Momentum in x direction:

$$\frac{\partial(\rho_{\mathrm{m}}u)}{\partial t}-\frac{\partial(\rho_{\mathrm{m}}u_0u)}{\partial x}+\frac{\partial(\rho_{\mathrm{m}}uu)}{\partial x}+\frac{\partial(\rho_{\mathrm{m}}vu)}{\partial y}+\frac{\partial(\rho_{\mathrm{m}}wu)}{\partial z}=-\frac{\partial p}{\partial x}+\frac{\partial}{\partial x}\left(\mu_{\mathrm{m}}\frac{\partial u}{\partial x}\right)+\frac{\partial}{\partial y}\left(\mu_{\mathrm{m}}\frac{\partial u}{\partial y}\right)+\frac{\partial}{\partial z}\left(\mu_{\mathrm{m}}\frac{\partial u}{\partial z}\right)+Au+j_yB_z-j_zB_y \qquad \text{(Eq 11)}$$

Momentum in y direction:

$$\frac{\partial(\rho_{\mathrm{m}}v)}{\partial t}-\frac{\partial(\rho_{\mathrm{m}}u_0v)}{\partial x}+\frac{\partial(\rho_{\mathrm{m}}uv)}{\partial x}+\frac{\partial(\rho_{\mathrm{m}}vv)}{\partial y}+\frac{\partial(\rho_{\mathrm{m}}wv)}{\partial z}=-\frac{\partial p}{\partial y}+\frac{\partial}{\partial x}\left(\mu_{\mathrm{m}}\frac{\partial v}{\partial x}\right)+\frac{\partial}{\partial y}\left(\mu_{\mathrm{m}}\frac{\partial v}{\partial y}\right)+\frac{\partial}{\partial z}\left(\mu_{\mathrm{m}}\frac{\partial v}{\partial z}\right)+Av+j_zB_x-j_xB_z \qquad \text{(Eq 12)}$$

Momentum in z direction:

$$\frac{\partial(\rho_{\mathrm{m}}w)}{\partial t}-\frac{\partial(\rho_{\mathrm{m}}u_0w)}{\partial x}+\frac{\partial(\rho_{\mathrm{m}}uw)}{\partial x}+\frac{\partial(\rho_{\mathrm{m}}vw)}{\partial y}+\frac{\partial(\rho_{\mathrm{m}}ww)}{\partial z}=-\frac{\partial p}{\partial z}+\frac{\partial}{\partial x}\left(\mu_{\mathrm{m}}\frac{\partial w}{\partial x}\right)+\frac{\partial}{\partial y}\left(\mu_{\mathrm{m}}\frac{\partial w}{\partial y}\right)+\frac{\partial}{\partial z}\left(\mu_{\mathrm{m}}\frac{\partial w}{\partial z}\right)+Aw+j_xB_y-j_yB_x+\rho_{\mathrm{m}}g\beta(T-T_l) \qquad \text{(Eq 13)}$$

Energy:

$$\frac{\partial(\rho_m h)}{\partial t} - \frac{\partial(\rho_m u_0 h)}{\partial x} + \frac{\partial(\rho_m u h)}{\partial x} + \frac{\partial(\rho_m v h)}{\partial y} + \frac{\partial(\rho_m w h)}{\partial z} = \frac{\partial}{\partial x}\left(k_m \frac{\partial T}{\partial x}\right) + \frac{\partial}{\partial y}\left(k_m \frac{\partial T}{\partial y}\right) + \frac{\partial}{\partial z}\left(k_m \frac{\partial T}{\partial z}\right) - \frac{\partial(\rho_m \Delta H)}{\partial t} \quad \text{(Eq 14)}$$

where ρ_m, k_m, μ_m, $C_{p,m}$, and σ_m are the density, thermal conductivity, viscosity, specific heat, and electrical conductivity of the workpiece, respectively. u, v, w are the velocities in x, y, z directions. j_x, j_y, j_z are the current densities in x, y, z directions. u_0 is the welding speed, T is the temperature, and t is time. The latent heat content ΔH in Eq 14 is given as $\Delta H = L f_l$. The constant $A = -C(1 - f_l)^2/(f_l^3 + b)$ in Eq 11-13 represent the porous medium model of the mushy region at the solid-liquid interface. The liquid fraction f_l is assumed to vary linearly with temperature (Ref 22):

$$f_l = \begin{cases} 0, & T < T_s \\ \dfrac{T - T_s}{T_l - T_s}, & T_s \le T \le T_l \\ 1, & T > T_l \end{cases} \quad \text{(Eq 15)}$$

Current continuity equation:

$$\frac{\partial}{\partial x}\left(\sigma_m \frac{\partial \phi}{\partial x}\right) + \frac{\partial}{\partial y}\left(\sigma_m \frac{\partial \phi}{\partial y}\right) + \frac{\partial}{\partial z}\left(\sigma_m \frac{\partial \phi}{\partial z}\right) = 0 \quad \text{(Eq 16)}$$

According to the above welding arc model's analysis for the electromagnetic field, the following equations are used in the 3D weld pool model (Ref 23).

$$j_x = -\sigma_m \frac{\partial \phi}{\partial x}, \quad j_y = -\sigma_m \frac{\partial \phi}{\partial y}, \quad j_z = -\sigma_m \frac{\partial \phi}{\partial z}. \quad \text{(Eq 17)}$$

$$\frac{\partial^2 A_x}{\partial x^2} + \frac{\partial^2 A_x}{\partial y^2} + \frac{\partial^2 A_x}{\partial z^2} + \mu_0 j_x = 0 \quad \text{(Eq 18)}$$

$$\frac{\partial^2 A_y}{\partial x^2} + \frac{\partial^2 A_y}{\partial y^2} + \frac{\partial^2 A_y}{\partial z^2} + \mu_0 j_y = 0 \quad \text{(Eq 19)}$$

$$\frac{\partial^2 A_z}{\partial x^2} + \frac{\partial^2 A_z}{\partial y^2} + \frac{\partial^2 A_z}{\partial z^2} + \mu_0 j_z = 0 \quad \text{(Eq 20)}$$

$$B_x = \frac{\partial A_z}{\partial y} - \frac{\partial A_y}{\partial z}, \quad B_y = \frac{\partial A_x}{\partial z} - \frac{\partial A_z}{\partial x}, \quad B_z = \frac{\partial A_y}{\partial x} - \frac{\partial A_x}{\partial y} \quad \text{(Eq 21)}$$

where A_x, A_y, A_z are the electrical vector potentials in x, y, z directions.

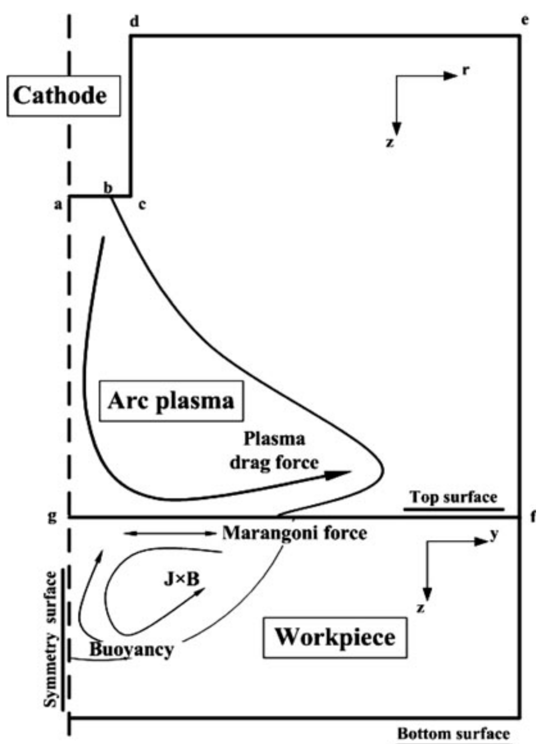

Fig. 1 A schematic plot of the weld cross section showing boundary conditions used in the calculation

2.3 Boundary Conditions

A 3D Cartesian coordinate system for the weld pool is used in the calculation, while only half of the workpiece is considered since the weld is symmetrical about the weld centreline. Figure 1 is a schematic plot showing the boundary conditions for welding arc and workpiece.

2.3.1 Welding Arc. The corresponding boundary conditions are summarized in Table 1. The most critical boundary condition is the electrical potential ϕ at the cathode spot (region a-b). The current density at the cathode spot, J_C, with a constant

Table 1 Boundary conditions for the welding arc model

	p	v_z	v_r	T	ϕ	A_z	A_r
ab	···	0	0	3000 Q = Eq 22	$\frac{\partial \phi}{\partial z} = J_C$	$\frac{\partial A_z}{\partial z} = 0$	$\frac{\partial A_r}{\partial z} = 0$
bc	···	0	0	3000	$\frac{\partial \phi}{\partial z} = 0$	$\frac{\partial A_z}{\partial z} = 0$	$\frac{\partial A_r}{\partial z} = 0$
cd	···	0	0	3000	$\frac{\partial \phi}{\partial r} = 0$	$\frac{\partial A_z}{\partial r} = 0$	$\frac{\partial A_r}{\partial r} = 0$
de	1	$\frac{\partial v_z}{\partial z} = 0$	$\frac{\partial v_r}{\partial z} = 0$	1000	$\frac{\partial \phi}{\partial z} = 0$	$\frac{\partial A_z}{\partial z} = 0$	$\frac{\partial A_r}{\partial z} = 0$
ef	1	$\frac{\partial v_z}{\partial r} = 0$	$\frac{\partial v_r}{\partial r} = 0$	1000	$\frac{\partial \phi}{\partial r} = 0$	$\frac{\partial A_z}{\partial r} = 0$	$\frac{\partial A_r}{\partial r} = 0$
fg	···	0	0	1000 Q = Eq 25	0	$\frac{\partial A_z}{\partial z} = 0$	$\frac{\partial A_r}{\partial z} = 0$
ga	···	$\frac{\partial v_z}{\partial r} = 0$	$\frac{\partial v_r}{\partial r} = 0$	$\frac{\partial T}{\partial r} = 0$	$\frac{\partial \phi}{\partial r} = 0$	$\frac{\partial A_z}{\partial r} = 0$	$\frac{\partial A_r}{\partial r} = 0$

The unit for pressure (p), velocity (v_z, v_r), temperature (T), and potential (ϕ) is atm, m/s, K and V, respectively value of 6.5×10^7 A/m^2 (Ref 24), is used as a flux for ϕ. The electric potential is assumed to be iso-potential (zero) at the anode (region f-g). This is based on the assumption that the conductivity in the metal is much higher than that in the plasma, implying that the variation of the electric potential in the metal is much less than that in the arc.

Besides setting the value of the temperature at the cathode surface, the presence of a voltage drop (known as cathode fall) is associated with a heat flux expressed by (Ref 19)

$$Q_C = |J_C| V_C \quad \text{(Eq 22)}$$

and the cathode voltage fall, V_C, can be described as

$$V_C = \frac{5k_B}{2\,e} T_{elec} \quad \text{(Eq 23)}$$

where T_{elec} is approximated by the following relationship:

$$T_{elec} = T_{c,g} - T_{cat} \quad \text{(Eq 24)}$$

where $T_{c,g}$ is the temperature of the argon gas in the cell closest to the cathode and T_{cat} is the temperature in the cathode.

A special treatment is required for the anode surface. Three principal modes of heat transfer contribute to the anode: (1) heat flux due to the electron flow Q_e, (2) conduction from the plasma Q_c, and (3) radiation from the plasma Q_r. Heat loss due to vaporization in the anode boundary is neglected. The calculating details can be found in Ref 25:

$$Q_A = Q_e + Q_c + Q_r. \quad \text{(Eq 25)}$$

2.3.2 Weld Pool. At all surfaces, we set the vector potential components flux to zero. The boundary conditions for the other variables are further discussed as follows.

Top Surface. The velocity boundary condition is given as

$$\tau = \tau_{s,t} + \tau_{gas} \quad \text{(Eq 26)}$$

where τ_{gas} is the shear stress of argon gas which is calculated from the arc model and $\tau_{s,t}$ is the Marangoni effect which is due to the variation of the surface tension with temperature and is described by

$$-\mu_m \frac{\partial u}{\partial z} = \frac{\partial \gamma}{\partial T}\frac{\partial T}{\partial x} \quad \text{(Eq 27)}$$

$$-\mu_m \frac{\partial v}{\partial z} = \frac{\partial \gamma}{\partial T}\frac{\partial T}{\partial y} \quad \text{(Eq 28)}$$

The temperature-dependent surface tension is obtained from a semi-empirical treatment given by Sahoo et al. (Ref 26):

$$\frac{\partial \gamma}{\partial T} = -A_\gamma - R\Gamma_s \ln\left(1 + K_{seg} a_i\right) - \frac{K_{seg} a_i}{1 + K_{seg} a_i}\frac{\Gamma_s \Delta H^\circ}{T} \quad \text{(Eq 29)}$$

$$K_{seg} = k_l \exp\left(-\frac{\Delta H^\circ}{RT}\right) \quad \text{(Eq 30)}$$

where $\partial\gamma/\partial T$ is the temperature coefficient of the surface tension, $\partial T/\partial x$ and $\partial T/\partial y$ are the temperature gradients in x, y directions. A_γ is the negative of $\partial\gamma/\partial T$ for pure metals (0.00043 N/m/K), Γ_s is the surface excess at saturation (1.3×10^{-8} J/kg/mol/m^2), R is the gas constant (8314.3 J/kg/mol/K), K_{seg} is the adsorption coefficient, k_l is the constant related to entropy of segregation (0.00318), ΔH° is the standard heat of absorption (-1.88×10^8 J/kg/mol), and a_i is the activity of oxygen (~wt.% O).

The heat flux at the top surface is given as

$$-k_m \frac{\partial T}{\partial z} = q_{arc} - \sigma_b \varepsilon\left(T^4 - T_a^4\right) - h_c(T - T_a) \quad \text{(Eq 31)}$$

where T_a is the surrounding temperature (300 K), σ_b is the Stefan-Boltzmann constant (5.67×10^{-8} W/m^2/K^4), ε is the radiation emissivity (0.4), h_c is the convective heat transfer coefficient (80 W/m/K), and q_{arc} is the heat flux that is calculated from the arc model. The second and third terms represent the heat loss by radiation and convection, respectively.

For the electric potential, there is a current density that is also obtained from the arc model.

Symmetry Surface. The boundary conditions are defined as zero flux across the symmetric surface as

$$\frac{\partial T}{\partial y} = 0, \quad \frac{\partial u}{\partial y} = 0, \quad \frac{\partial w}{\partial y} = 0, \quad v = 0, \quad \frac{\partial \phi}{\partial y} = 0 \quad \text{(Eq 32)}$$

Other Surfaces. At all other surfaces, temperatures are set at ambient temperature and the velocities are set to be zero. The bottom boundary for the electric potential is electrically isolated and hence the current density at this boundary is zero. For the side surface, since the electrical conductivity of the metal is very high and this boundary is far enough from the weld pool surface, it is assumed that the electric potential at this surface is zero and independent of the distance from surface.

2.4 Material Properties for the Gas and Workpiece

Welding shield gas is argon. Thermophysical properties of argon are taken from the tabulated data of Boulos et al. (Ref 27). The radiation loss term S_R for argon in the energy conservation equation is taken from experimental data of Evans and Tankin (Ref 28). Calculations have been performed for an SUS304 stainless steel. The thermodynamic and transport properties of this alloy are considered to be constant and derived from Ref 29 and 30.

2.5 Numerical Treatment

For the workpiece, a nonuniform grid point system is employed with finer grid sizes near the weld pool region to improve the computation accuracy because of the higher temperature and velocity gradients. A $100 \times 30 \times 30$ grid points was utilized for the computational domain of 100 mm × 25 mm × 10 mm, and the origin of the calculation is located at the center of the block. In the arc region, these grid points are refined on the axis of the discharge and near the electrodes surface. The smallest grids are the thickness of the anode fall region (0.1 mm × 0.1 mm). The system of partial differential equations which constitutes the model is discretized and solved iteratively by the segregated solver of the CFD commercial FLUENT© code, enhanced with dedicated UDF to handle the source terms and the extra scalar equations needed for the electromagnetic variables (Ref 31). The standard SIMPLE algorithm (Ref 32) is used for the pressure-velocity coupling, and a second-order interpolation scheme is employed in all the equations of the model.

To obtain rapid convergence to decrease the calculation time, the best combination of the some remedies including increasing the number of cells, decreasing the time intervals, and utilizing the under-relaxation factor was determined by trial and error. Calculations were executed on PC Dell 3 GB, and it took about 40 h of CPU time to perform a typical analysis.

3. Results and Discussion

3.1 Simulation for Welding Arc

To verify the validity of the welding arc model, the results of the calculations are compared with available experimental data. Hsu et al. (Ref 33) and Nestor (Ref 34) reported experimental measurements of temperature fields for argon welding arcs together with heat flux and current density distributions at the anode.

Figure 2 shows both the calculated (on the right) and experimental (Ref 33) (on the left) temperature contours of argon arc for 200 A welding current and 10 mm arc length. Comparisons between the calculated and the measured temperature distributions show good agreement when the temperature is over 12,000 K. The cooler arc fringe with a temperature of below 12,000 K, where sharp temperature drop and steep charged partial concentration exist, deviated significantly from the observed fringe possibly due to the LTE assumption not being as valid as it is at higher temperature. A typical bell shape of the arc periphery, expressed by the isotherm of 11,000 K, is observed. In addition, Fig. 3(a) and (b) show the calculated anode heat flux and current density of argon arc compared with experiments (Ref 34) at 200 A welding current and 6.3 mm arc length. It should be evident that the numerical results agree well with the experimental data.

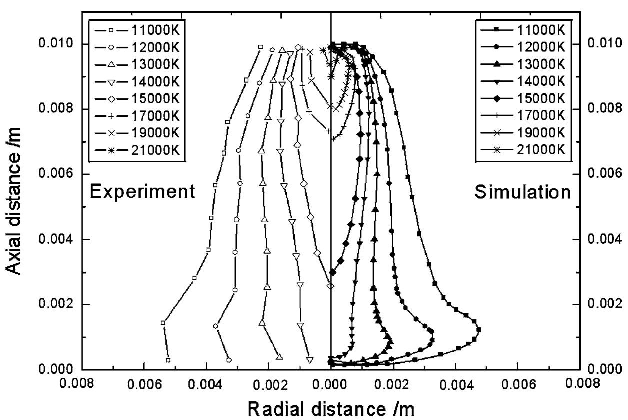

Fig. 2 Comparison between experimental and calculated temperature contours in the welding arc for argon arc. The experimental results are from Hsu et al. (Ref 33)

To consider and analyze the effect of plasma drag force on the weld pool shape, under welding current of 160 A with 3 mm arc length, the heat flux, current density, and shear stress on the anode surface are calculated as shown in Fig. 4.

3.2 Simulation for Weld Pool

According to the experimental results (Ref 35), oxygen-added argon shielding gas can dramatically increase the weld D/W ratio to 0.5 when the oxygen concentration is in the range of 3000 to 5000 ppm. Too high or low oxygen addition content will decrease the D/W ratio to approximately 0.2. The oxygen in the weld remains nearly constant when the oxygen addition content is over 6000 ppm. In this study, the oxygen addition content in shielding gas is selected from 1000 to 5000 ppm. The corresponding oxygen content in the weld is 30, 50, 130, 175, and 220 ppm. The corresponding welding parameter is as follows: welding current 160 A, arc length 3 mm, and welding speed 2 mm/s.

3.2.1 Weld Shape Under Different Oxygen Contents. The calculated velocity vectors and temperature fields for the weld containing 50 and 175 ppm of oxygen are presented in Fig. 5 and 6, respectively. The simulated results clearly show that there are three vortexes at *xz* face and two vortexes at *yz* face. At *xz* face, the first vortex is clockwise on the foreside of the weld pool, the second vortex is counterclockwise at the center of the weld pool, and the third vortex is clockwise at the end of the weld pool. At *yz* face, the first vortex is clockwise near the centerline of the weld pool; the other vortex is counterclockwise near the periphery of the weld pool. However, the size of these vortexes has a significant difference with different oxygen contents. For the oxygen content of 50 ppm, the vortex (outward direction) at the center of the weld pool is larger than the others, and the heat from arc is efficiently transferred to the weld periphery and produces a

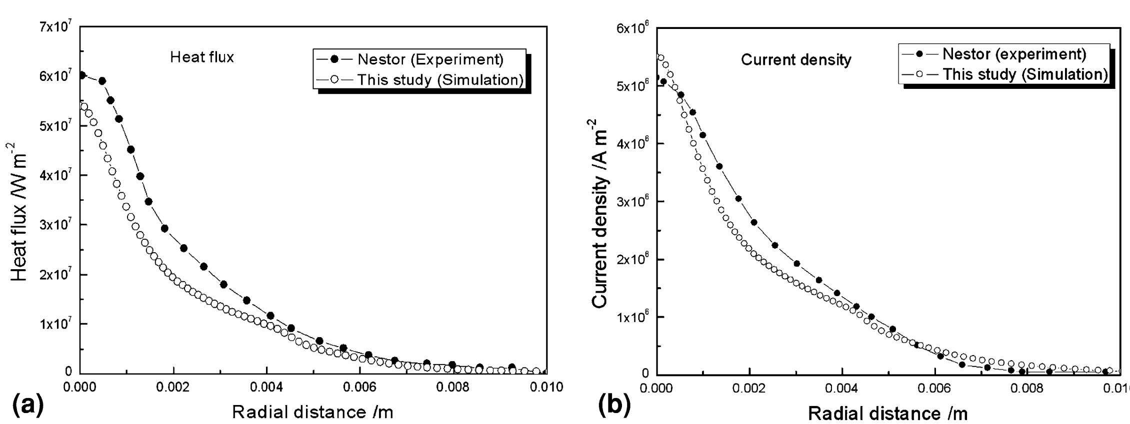

Fig. 3 Comparison between experimental and calculated anode heat flux (a) and current density (b) distribution for argon arc. The experimental results are from Nestor (Ref 34)

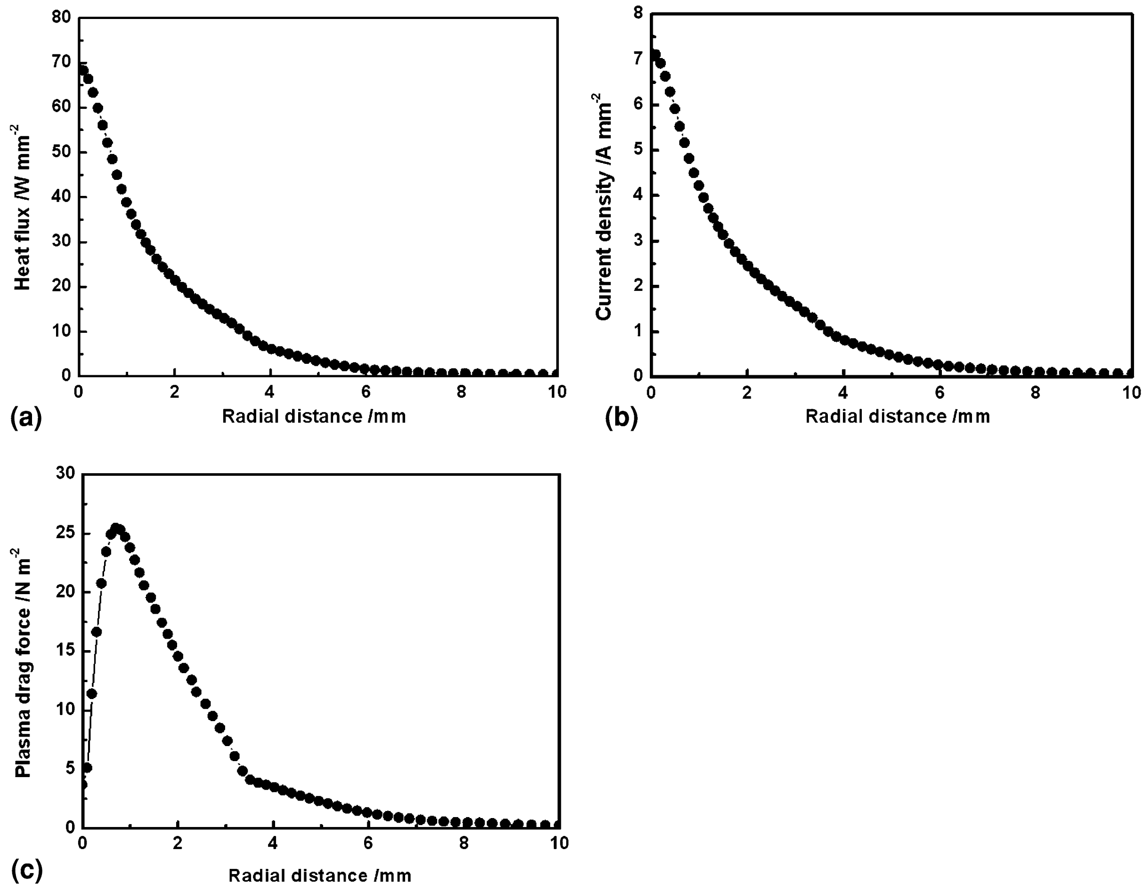

Fig. 4 Calculation results: (a) heat flux, (b) current density and (c) plasma drag force on the anode surface from welding arc model

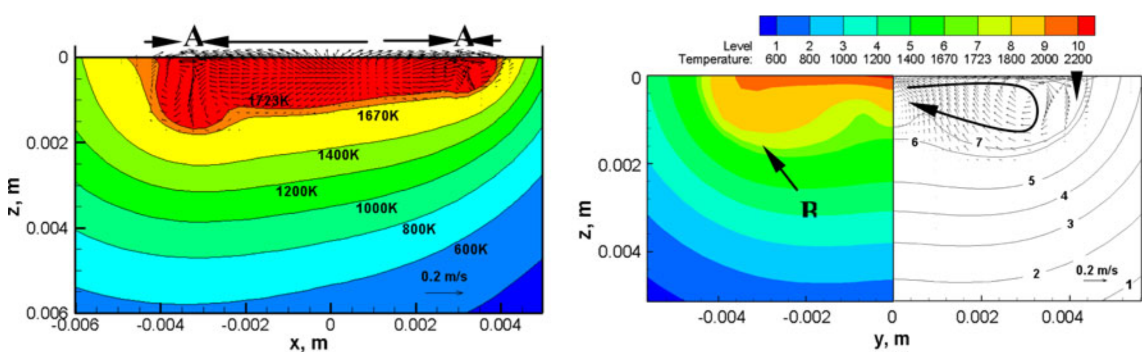

Fig. 5 Temperature and velocity fields with low oxygen (50 ppm)

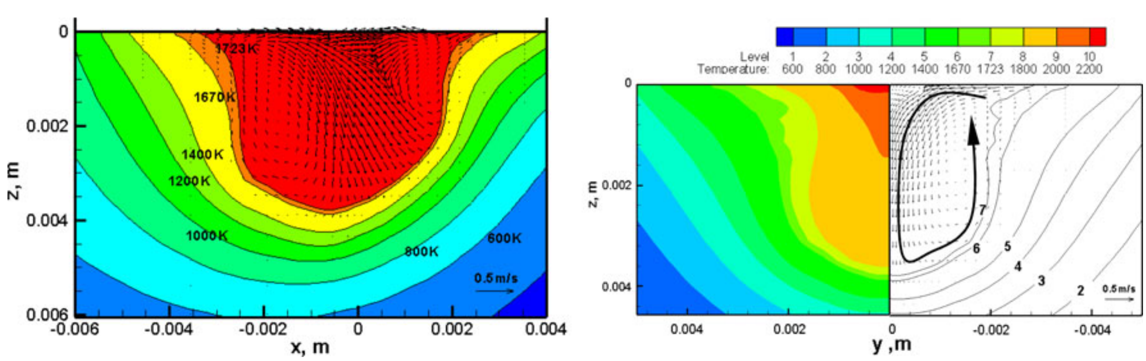

Fig. 6 Temperature and velocity fields with high oxygen (175 ppm)

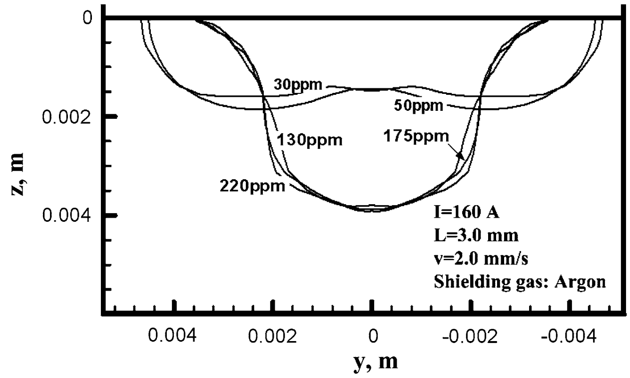

Fig. 7 Weld shapes (yz face) with different oxygen contents

relatively wide and shallow penetration. As the oxygen content is 175 ppm, there are two vortexes whose directions are flowing from the edge toward the center. The two flows meet at the region on the free surface near the center, and carry the heat flux heat downward from the arc to the bottom and create a deep and narrow penetration.

Figure 7 shows the predicted weld cross-sections (*yz* face) under different oxygen contents. It is clearly shown that the weld width decreases and the weld depth increases with the increasing oxygen content, which indicates that the convection mode in the liquid pool is completely changed with the increasing of oxygen content from 50 to 130 ppm.

3.2.2 Fe-O Surface Tension and Marangoni Convection of Molten Pool. As shown in Fig. 5 to 7, the weld metal oxygen content can significantly change the weld shape. The surface active elements such as sulfur, oxygen, and selenium in the weld pool can change the sign of the temperature coefficient of the surface tension when their content is over a critical value (Ref 6, 7). Sahoo et al. (Ref 26) calculated values for γ and $\partial\gamma/\partial T$ for the Fe-O system and values of the temperature coefficient is given in Fig. 8. It can be seen that the temperature coefficient of the surface tension depends both on the oxygen content and the weld pool surface temperature. It is interesting to note that at the same oxygen content, $\partial\gamma/\partial T$ can change from a positive value at relatively low temperatures to a negative value at higher temperatures. This implies that as the weld pool surface temperature is increased from the pool edge to the pool center, $\partial\gamma/\partial T$ may go through an inflection point somewhere on the surface of the pool. When the temperature coefficient of the surface tension on the molten pool is in negative value, $\partial\gamma/\partial T < 0$, the surface tension is higher in the relatively cooler part of the pool edge than that in the pool center area under the arc, and hence, this surface tension gradient will introduce the outward Marangoni convection. Under the outward Marangoni convection, the heat flux is easily transferred from the pool center to the edge, and makes the weld shape wide and shallow as shown in Fig. 5. When the temperature coefficient of the surface tension changes from a negative to positive value, $\partial\gamma/\partial T > 0$, the direction of Marangoni convection in the molten pool is in inward direction as illustrated in Fig. 6. In this case, the heat flux is easily transferred from the pool center to the pool bottom, and makes the weld shape narrow and deep.

For a weld metal oxygen content of 30 ppm, according to Fig. 8, the critical temperature at the inflection point on the weld pool surface is approximately 1900 K. The temperature coefficient of the surface tension is positive when the surface temperature is lower than 1900 K. As the melt temperature increases beyond this temperature, the temperature coefficient of the surface tension becomes negative. Therefore, the positive $\partial\gamma/\partial T$ near the cooler periphery of the weld pool produces a radially inward flow, and the radially outward flow at the hotter center area of the weld pool is caused by negative $\partial\gamma/\partial T$. However, this periphery inward flow is relatively weak, and does not significantly influence the fluid flow or the overall heat transfer in the weld pool. Under this convection mode, the heat from the arc is carried by the outward flow, and the convective heat transport is consequently directed away from the axis, resulting in shallow wide weld shape, as shown in Fig. 5. Since there are inward (pool edge) and outward (pool center area) coexisting on the pool surface, an intersection point will exist on the periphery area A point (shown in Fig. 5). The heat flux will transfer from the pool center to pool edge and at the intersection point it will go downward, which make pool bottom with concave shape at the two sides (point B at Fig. 5).

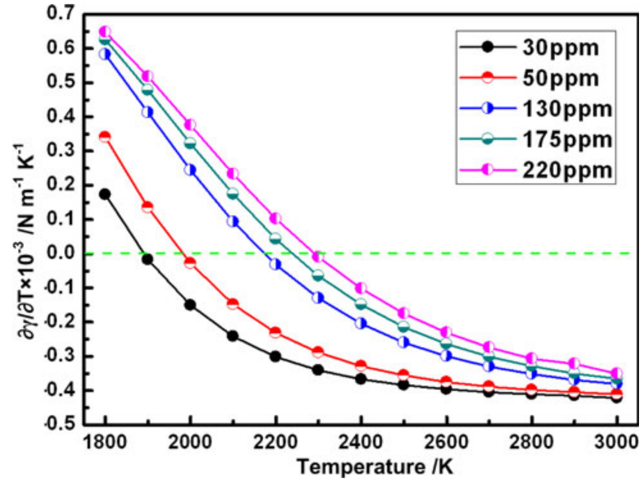

Fig. 8 Variation of temperature coefficient of surface tension of Fe-O systems as a function of oxygen concentration and temperature

As the weld metal oxygen content is increased, the critical temperature is increased as shown in Fig. 8. When the oxygen content is 175 ppm, the critical temperature is about 2250 K. The calculated results from this study show that the temperature of most of the weld pool surface is little lower than this temperature, and therefore, a positive $\partial\gamma/\partial T$ exists almost all over the weld pool surface. Even though there still exist opposing loops, the outward flow loop is considerably smaller than the inward flow loop and does not have any significant effect on the temperature field. Hence, large inward loops carry the heat flux downward from the arc to the bottom and create a deep and narrow penetration, as shown in Fig. 6.

3.3 Comparison Between Experiment and Calculation

Experimental researches are carried out by the addition of oxygen to the argon base shielding with oxygen content from 1000 to 5000 ppm (Ref 35). It provides a significant source of oxygen absorption for the weld pool, and changes the Marangoni convection direction in the weld pool, which makes the weld depth deeper. Figure 9 shows the comparison between experiment and calculation for the ratio of penetration depth to width (D/W). The weld D/W ratio increases first and then maintains constant with the increasing oxygen content. The experimental results' weld D/W ratio agrees quite well with the

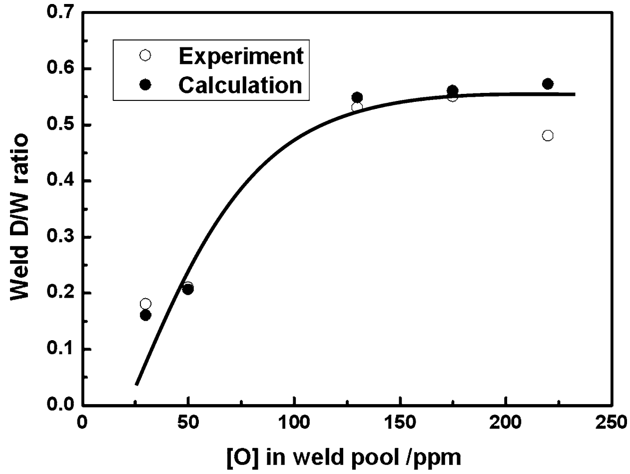

Fig. 9 Comparison between experiment and calculation for weld depth and width ratio

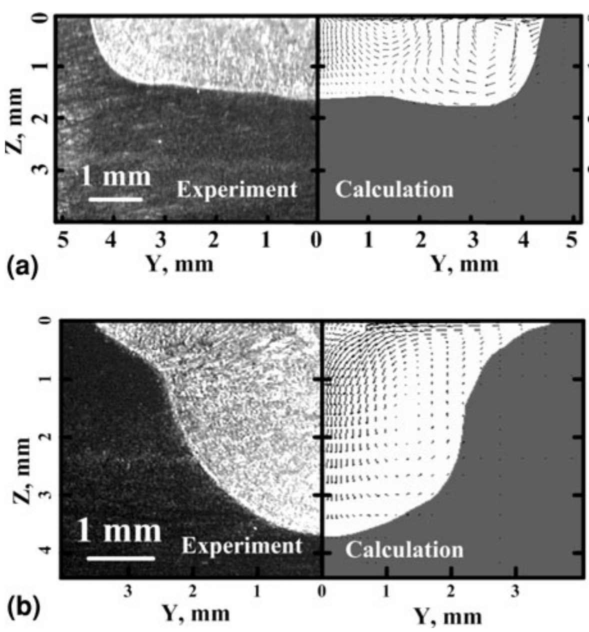

Fig. 10 Comparison between experimental and calculated weld profiles: (a) low oxygen (30 ppm) and (b) high oxygen (175 ppm)

simulation results. Figure 10 shows the predicted weld shapes, compared with experimental results, for both low (30 ppm) and high (175 ppm) oxygen in the weld. Both the experimental and simulated results indicate that the weld shape changes from a wide shallow to a narrow deep one when the oxygen varies from 50 to 130 ppm. At the same time, it can be found that when the plasma drag force from the welding arc is considered, both the weld shape and the size of the weld show good agreement between the experiment and the calculation.

4. Conclusions

(1) A numerical model of the welding arc, which is coupled to a model for the heat transfer and fluid flow in the weld pool of a SUS304 stainless steel during a moving GTA welding process, has been established. The calculated temperature distribution in the arc plasma, the calculated distribution of current density, and heat flux at the anode agree well with the existing experimental data.

(2) The calculated results indicate that the oxygen is a main surface active element for SUS304 stainless steel. When the oxygen content in the weld pool is over a critical value, which is between 50 and 130 ppm, the Marangoni convection model in the weld pool will be changed from outward to inward direction, which makes the shallow wide weld shape to the narrow deep one. The weld D/W ratio increases first and then maintains constant with the increasing oxygen content.

(3) Marangoni convection is one of the main factors that influence the heat transfer in the weld pool. Based on the Marangoni force, the weld shape could be simulated accurately by considering the arc plasma drag force on the weld pool, which was numerically obtained from welding arc model.

Acknowledgments

The authors are grateful for the financial support from the National Science Foundation of China (NSFC) under Grant No. 50874101 and the Science Program of Shenyang City under Grant No. 1071275-0-02.

References

1. S.M. Gurevich and V.N. Zamkov, Nekotorye Osovennosti Svarki Titana Neplaviachinsia Zlektrodom S Primeneniem Flynsov, *Avtom. Svarka*, 1966, **12**, p 13–16
2. M.M. Savitskii and G.I. Leskov, Mechanizm Vliyamia Dzlektrootrida Tepvnykh Zpementov Na Proplavlauchyu Sposovnosti Luqi S Voliframoym Katodm, *Avtom. Svarka*, 1980, **9**, p 17–22
3. W. Lucas and D.S. Howse, Activating Flux-Increasing the Performance and Productivity of the TIG and Plasma Processes, *Weld. Metal Fabr.*, 1996, **64**, p 11–17
4. D.S. Howse and W. Lucas, Investigation into Arc Constriction by Active Fluxes for Tungsten Inert Gas Welding, *Sci. Technol. Weld. Join.*, 2000, **5**, p 189–193
5. D. Fan, R.H. Zhang, Y.F. Gu, and M. Ushio, Effect of Flux on A-TIG Welding of Mild Steel, *Trans. JWRI*, 2001, **30**, p 35–40
6. C.R. Heiple and J.R. Roper, Mechanism for Minor Effect on GTA Fusion Zone Geometry, *Weld. J.*, 1982, **61**, p 97s–102s
7. C.R. Heiple and J.R. Roper, Surface Active Element Effects on the Shape of GTA, Laser, and Electron Beam Welds, *Weld. J.*, 1983, **62**, p 72s–77s
8. M. Tanaka, T. Shimizu, H. Terasaki, M. Ushio, F. Koshi-ishi, and C.L. Yang, Effects of Activating Flux on Arc Phenomena in Gas Tungsten Arc Welding, *Sci. Technol. Weld. Join.*, 2000, **6**, p 397–402
9. P.J. Modenesi, E.R. Apolinario, and I.M. Pereira, TIG Welding with Single Component Fluxes, *J. Mater. Proc. Technol.*, 2000, **99**, p 260–265
10. S.P. Lu, H. Fujii, H. Sugiyama, M. Tanaka, and K. Nogi, Weld Penetration and Marangoni Convection with Oxide Fluxes in GTA Welding, *Mater. Trans.*, 2002, **43**, p 2926–2931
11. J.J. Lowke, M. Tanaka, and M. Ushio, Insulation Effects of Flux Layer in Producing Greater Weld Depth, *Proc. 57th Ann. Assembly Int. Inst. Weld.*, July 2004 (Osaka, Japan), International Institute of Welding, IIW Doc. 212-1053-04
12. G.M. Oreper and J. Szekely, A Comprehensive Representation of Transient Weldpool Development in Spot Welding Operations, *Metall. Trans. A*, 1987, **18**, p 1325–1332
13. T. Zacharia, S.A. David, J.M. Vitek, and T. Debroy, Weld Pool Development During GTA and Laser Beam Welding of Type 304 Stainless Steel, Part I. Theoretical Analysis, *Weld. J.*, 1989, **68**, p 499s–509s

14. T. Zacharia, S.A. David, J.M. Vitek, and T. Debroy, Weld Pool Development During GTA and Laser Welding of Type 304 Stainless Steel, Part II. Experimental Correlation, *Weld. J.*, 1989, **68**, p 510s–519s
15. Y. Wang, Q. Shi, and H.L. Tsai, Modeling of the Effects of Surface-Active Elements on Flow Patterns and Weld Penetration, *Metall. Mater. Trans. B*, 2001, **32**, p 145–161
16. R.H. Zhang and D. Fan, Effects of Activating Flux on Flow Patterns and Weld Penetration in ATIG Welding, *Sci. Technol. Weld. Join.*, 2007, **12**(1), p 15–23
17. W.C. Dong, S.P. Lu, D.Z. Li, and Y.Y. Li, Numerical Simulation of Effects of the Minor Active-Element Oxygen on the Marangoni Convection and the Weld Shape, *Acta Metall. Sin.*, 2008, **44**, p 249–256 (in Chinese)
18. M. Tanaka, H. Terasaki, M. Ushio, and J.J. Lowke, Numerical Study of a Free-Burning Argon Arc with Anode Melting, *Plasma Chem. Plasma Process.*, 2003, **23**(3), p 585–606
19. M.A. Ramirez, G. Trapaga, and J. McKelliget, A Comparison Between Two Different Numerical Formulations of Welding Arc Simulation, *Model. Simul. Mater. Sci. Eng.*, 2003, **11**, p 675–695
20. F. Lago, J.J. Gonzalez, P. Freton, and A. Gleizes, A Numerical Modeling of an Electrode Arc and Its Interaction with the Anode: Part I. The Two-Dimensional Model, *J. Phys. D Appl. Phys.*, 2004, **37**, p 883–897
21. Y.M. Zhang, Z.N. Cao, and R. Kovacevic, Numerical Analysis of Fully Penetrated Weld Pools in GTA Welding, *Proc. Inst. Mech. Eng., Part C. J. Mech. Eng. Sci.*, 1996, **210**, p 187–195
22. V.R. Voller, M. Cross, and N.C. Markatos, An Enthalpy Method for Convection Diffusion Phase-Change, *Int. J. Numer. Methods Eng.*, 1987, **24**, p 271–284
23. J.J. Gonzalez, F. Lago, P. Freton, M. Masquere, and X. Franceries, Numerical Modelling of an Electric Arc and Its Interaction with the Anode: Part II. The Three-Dimensional Model-Influence of External Forces on the Arc Column, *J. Phys. D Appl. Phys.*, 2005, **38**, p 306–318
24. J. McKelliget and J. Szekely, Heat Transfer and Fluid Flow in the Welding Arc, *Metall. Mater. Trans. A*, 1986, **17**, p 1139–1148
25. C.S. Wu and J.Q. Gao, Analysis of the Heat Flux Distribution at the Anode of a TIG Welding Arc, *Comput. Mater. Sci.*, 2002, **24**(3), p 323–327
26. P. Sahoo, T. DebRoy, and M.J. McNallan, Surface Tension of Binary Metal-Surface Active Solute Systems Under Conditions Relevant to Welding Metallurgy, *Metall. Trans. B*, 1988, **19**, p 483–491
27. M.I. Boulos, P. Fauchais, and E. Pfender, *Thermal Plasmas—Fundamentals and Applications*, Vol 1, Plenum, New York, 1994, p 388
28. D.L. Evans and R.S. Tankin, Measurement of Emission and Absorption of Radiation by an Argon Plasma, *Phys. Fluids*, 1967, **10**(6), p 1137–1144
29. R.T.C. Choo, J. Szekely, and S.A. David, On the Calculation of the Free Surface Temperature of Gas-Tungsten-Arc Weld Pools from First Principles: Part II. Modeling the Weld Pool and Comparison with Experiments, *Metall. Trans. B*, 1992, **23**, p 371–384
30. H.G. Fan, H.L. Tsai, and S.J. Na, Heat Transfer and Fluid Flow in a Partially or Fully Penetrated Weld Pool in Gas Tungsten Arc Welding, *Int. J. Heat Mass Transfer*, 2001, **44**, p 417–428
31. Fluent Inc., *FLUENT User's Manual*, Lebanon, NH, 2005
32. S.V. Patankar, *Numerical Heat Transfer and Fluid Flow*, McGraw-Hill, New York, 1980
33. K.C. Hsu, K. Etemadi, and E. Pfender, Study of the Free-Burning High-Intensity Argon Arc, *J. Appl. Phys.*, 1982, **54**(3), p 1293–1301
34. O.H. Nestor, Heat Intensity and Current Density Distributions at the Anode of High Current, Inert Gas Arcs, *J. Appl. Phys.*, 1962, **33**(5), p 1638–1648
35. S.P. Lu, H. Fujii, H. Sugiyama, M. Tanaka, and K. Nogi, Effects of Oxygen Additions to Argon Shielding Gas on GTA Weld Shape, *ISIJ Int.*, 2003, **43**(10), p 1590–1595